

Relative Contributions of Intraocular and Cerebrospinal Fluid Pressures to the Biomechanics of the Lamina Cribrosa and Laminar Neural Tissues

Alireza Karimi,¹ Reza Razaghi,¹ Seyed Mohammadali Rahmati,² Christopher A. Girkin,¹ and J. Crawford Downs¹

¹Department of Ophthalmology and Visual Sciences, University of Alabama at Birmingham, Birmingham, Alabama, United States

²School of Biological Sciences, Georgia Institute of Technology, Atlanta, Georgia, United States

Correspondence: J. Crawford Downs, Department of Ophthalmology and Visual Sciences, University of Alabama at Birmingham, 1670 University Boulevard, VH 390A, Birmingham, AL 35294, USA; cdowns@uabmc.edu.

Received: May 13, 2022

Accepted: September 27, 2022

Published: October 18, 2022

Citation: Karimi A, Razaghi R, Rahmati SM, Girkin CA, Downs JC. Relative contributions of intraocular and cerebrospinal fluid pressures to the biomechanics of the lamina cribrosa and laminar neural tissues.

Invest Ophthalmol Vis Sci. 2022;63(11):14.

<https://doi.org/10.1167/iovs.63.11.14>

<https://doi.org/10.1167/iovs.63.11.14>

PURPOSE. The laminar region of the optic nerve head (ONH), thought to be the site of damage to the retinal ganglion cell axons in glaucoma, is continuously loaded on its anterior and posterior surfaces by dynamic intraocular pressure (IOP) and orbital cerebrospinal fluid pressure (CSFP), respectively. Thus, translaminar pressure (TLP; TLP = IOP-CSFP) has been proposed as a glaucoma risk factor.

METHODS. Three eye-specific finite element models of the posterior human eye were constructed, including full 3D microstructures of the load-bearing lamina cribrosa (LC) with interspersed laminar neural tissues (NTs), and heterogeneous, anisotropic, hyperelastic material formulations for the surrounding peripapillary sclera and adjacent pia. ONH biomechanical responses were simulated using three combinations of IOP and CSFP loadings consistent with posture change from sitting to supine.

RESULTS. Results show that tensile, compressive, and shear stresses and strains in the ONH were higher in the supine position compared to the sitting position ($P < 0.05$). In addition, LC beams bear three to five times more TLP-driven stress than interspersed laminar NT, whereas laminar NT exhibit three to five times greater strain than supporting LC ($P < 0.05$). Compared with CSFP, IOP drove approximately four times greater stress and strain in the LC, NT, and peripapillary sclera, normalized per mm Hg pressure change. In addition, IOP drove approximately three-fold greater scleral canal expansion and anterior-posterior laminar deformation than CSFP per mm Hg ($P < 0.05$).

CONCLUSIONS. Whereas TLP has been hypothesized to play a prominent role in ONH biomechanics, the IOP and CSFP effects are not equivalent, as IOP-driven stress, strain, and deformation play a more dominant role than CSFP effects.

Keywords: posture, intraocular pressure (IOP), cerebrospinal fluid pressure (CSFP), optic nerve head (ONH), finite element, ocular biomechanics

Intraocular pressure (IOP) elevation is one of the primary risk factors for primary open-angle glaucoma.^{1,2} Although the mechanisms underlying how IOP leads to the loss of retinal ganglion cell function in glaucoma is not completely understood, it has been proposed that biomechanical, vascular, and cellular pathways in the optic nerve head (ONH) region are involved.³⁻⁵ IOP induces biomechanical strain in the load-bearing lamina cribrosa (LC) and interspersed laminar neural tissues (NTs; resident glial cells and the retinal ganglion cell axons), and it has been hypothesized that increased strain, as well as its downstream vascular and cellular effects, leads to apoptosis of the ganglion cells and subsequent loss of vision.^{3,4,6-8} Emerging evidence suggests that cerebrospinal fluid pressure (CSFP) may also play a role in glaucoma pathogenesis and progression, with several retrospective clinical studies indicating that patients with elevated CSFP are less likely to develop glaucoma, and patients with low CSFP are more likely to suffer glau-

coma damage,^{9,10} although some studies have suggested otherwise.¹¹ A recent prospective study confirmed these findings,¹²⁻¹⁴ which has also been suggested by an optic neuropathy induced by CSFP-lowering in the nonhuman primate (NHP).¹⁵ Many investigators have hypothesized that IOP and CSFP combine to influence ONH biomechanics, and that biomechanics is the pathway through which these pressures contribute to glaucoma. The relationship between IOP and glaucoma has been studied extensively because it can be measured in patients noninvasively, but less is known about CSFP because there is no accurate noninvasive measurement technique. In addition, whereas it has been assumed in these studies that IOP and CSFP are controlled independently, recent experimental studies indicate that IOP and CSFP are positively coupled via neural pathways, which could complicate the interpretation of prior published results if this finding translates to humans.¹⁶ Several reviews have outlined the evidence supporting the

view that CSFP is important in glaucoma, in addition to IOP.^{17–20}

The LC forms a barrier between the intraocular and the retrobulbar optic nerve tissue compartments,^{21–23} and has been identified as the likely site of damage to the retinal ganglion cell axons in glaucoma.^{7,24,25} Mechanical strain has been implicated in the potential damage processes in both axons and astrocytes in the ONH.^{26–29} IOP acts on the LC and ONH from inside the eye (anterior) and CSFP counteracts IOP from the posterior LC through the translaminar pressure (TLP; $TLP = IOP - CSFP$).^{5,19,21–23,30,31} It is important to note that whereas IOP acts directly on the entire globe, and hence the LC and sclera, CSFP envelops the retrobulbar optic nerve and only counteracts IOP at the LC. Hence, the TLP generates mechanical force and deformation in the neural and connective tissues and central retinal vessels in the lamellar region.^{32–34} The retrolaminar tissue compartment is constrained by the load-bearing pia mater around the optic nerve, resulting in significant positive retrolaminar tissue pressure that is similar to the surrounding CSFP in the subarachnoid space.³⁰

It has been well documented that TLP varies with postural transition from the sitting to the supine position.^{35–41} In these studies, postural change elicited a greater change in CSFP compared with IOP. The role of simultaneous changes in IOP and CSFP^{42–48} on ONH biomechanics has been studied both experimentally and computationally.^{49–54} However, these studies considered the neural and connective tissues in the lamellar region as a single homogenous material. Hence, little is known about how TLP alteration with change in body position affects the biomechanics of the LC beams themselves and the interspersed lamellar NT. Experimental studies^{23,48,55,56} investigating the ONH biomechanical environment and response due to TLP and the TLP gradient have greatly contributed in our understanding of ONH biomechanics. However, either most of these studies considered the IOP and/or CSFP separately,^{23,55} or experimental limitations prevented the measurement of strains in the LC beams and NT separately.^{48,56} Separating the stresses and strains in the LC beams from that of the contained axons is critical, as these strains likely drive remodeling of LC morphology and mechanical properties^{8,57–59} and could damage the interspersed retinal ganglion cell axons.^{60,61} This is crucial for understanding how IOP- and CSFP-related stresses and strains influence the changes in structural support for the retinal ganglion cell axons in the lamellar region.

The impact of simultaneous IOP and CSFP elevation on both the LC beam and lamellar NT stresses and strains remain unknown due to the limitations of prior approaches. In this study, three eye-specific finite element (FE) models that included the full 3D LC and NT microstructures were constructed⁶²; circumferential, radial, and planar isotropic cable elements were distributed in the sclera and pia to represent the directional stiffness imparted by anisotropic collagen fibril orientation in those tissues. The cable elements were coupled with the solid scleral and pia matrixes using a fully coupled mesh-free, penalty-based beam-in-solid material-modeling algorithm.⁶³ Three different IOP and CSFP load boundaries were applied to the FE models: the physiologic case in which both IOP and CSFP varies due to changes in body position, and two cases in which either IOP or CSFP was held constant to separate the independent biomechanical contributions of IOP and CSFP to TLP change. The results were interpreted in terms of the tensile, compressive, and shear stresses and strains in the

LC beams and lamellar NT, as well as scleral canal expansion and lamellar deformation.

MATERIALS AND METHODS

3D Eye-Specific FE Model of the Human Optic Nerve Head

In this study, we used eye-specific FE models of the posterior pole derived from high-fidelity 3D reconstructions of a human donor eye^{62–65} to simulate the role of the body position on the resultant stresses and strains within the individual ONH connective tissues. The construction of the models has been fully described in our previous publications.^{62–65} In brief, the ONH and peripapillary is defined by 3D delineation of anatomic tissue surfaces within a high-resolution, histologic, fluorescent 3D reconstruction of the posterior eye and ONH obtained from three human donor eyes intravitreally and immersion fixed while maintaining an IOP of 10 mm Hg and CSFP of 0 mm Hg.⁶⁶ Donors 118 (female, 40 years old), 119 (male, 79 years old), and 129 (female, 34 years old) were of European descent with ocular normality confirmed by ophthalmic clinical record review. Manually delineated 3D surfaces of the eye-specific geometries of the ONH and peripapillary sclera (PPScl) were then fit into a larger generic posterior scleral shell with anatomic shape and thickness.⁶² The Border Tissues of Elschnig and Jacoby are faithfully represented in the 3D geometries that are the basis of our models, and are meshed and modeled as part of the scleral solid. We are not aware of any studies reporting that the border tissues possess different mechanical properties than the adjacent sclera, and so they were assigned the same material parameters as the sclera. Finally, a parameterized, anatomic surface defining the anterior surface of the prelaminar NT and retina was added; note the choroid was neglected, because it was collapsed in the reconstructed enucleated eyes⁶² (Figs. 1a, 1b). The LC microstructure was segmented into a binary image volume from the original 12-bit grayscale images of the lamellar region using an automated segmentation algorithm designed for this purpose, as described previously.⁶⁷ The segmented LC was then meshed with eight-noded hexahedral elements using a custom Matlab (Mathworks, Natick, MA, USA) script that creates the mesh directly from the binary LC image volume, as described in our recent publication.⁶² The final volume mesh of the LC beams and interspersed NT were incorporated into the human ONH model, as shown in Figure 1b and described previously.⁶²

The heterogeneous anisotropic collagen fibril orientations that impart directional stiffness to the peripapillary sclera⁶⁸ and pia mater were represented with discrete, linear elastic cable elements embedded in the sclera (circumferential, radial, and planar isotropic) and pia (planar isotropic) using a custom MatLab code, as described in our recent publication⁶³ and shown in Figure 1c. The collagen fibers/cable elements were embedded in the solid matrix of the sclera and pia using a fully coupled mesh-free penalty-based beam-in-solid algorithm wherein the solid elements can be highly deformed by the 3D adaptive Element-Free-Galerkin solid formulation.^{69–73} A Gaussian function was used to smooth the directional transition between the circumferential, radial, and isotropic fiber/cable element regions in the peripapillary sclera, which results in smooth stress and strain patterns. The material parameters of all three eye-specific FE models are listed in Table 1. The solid

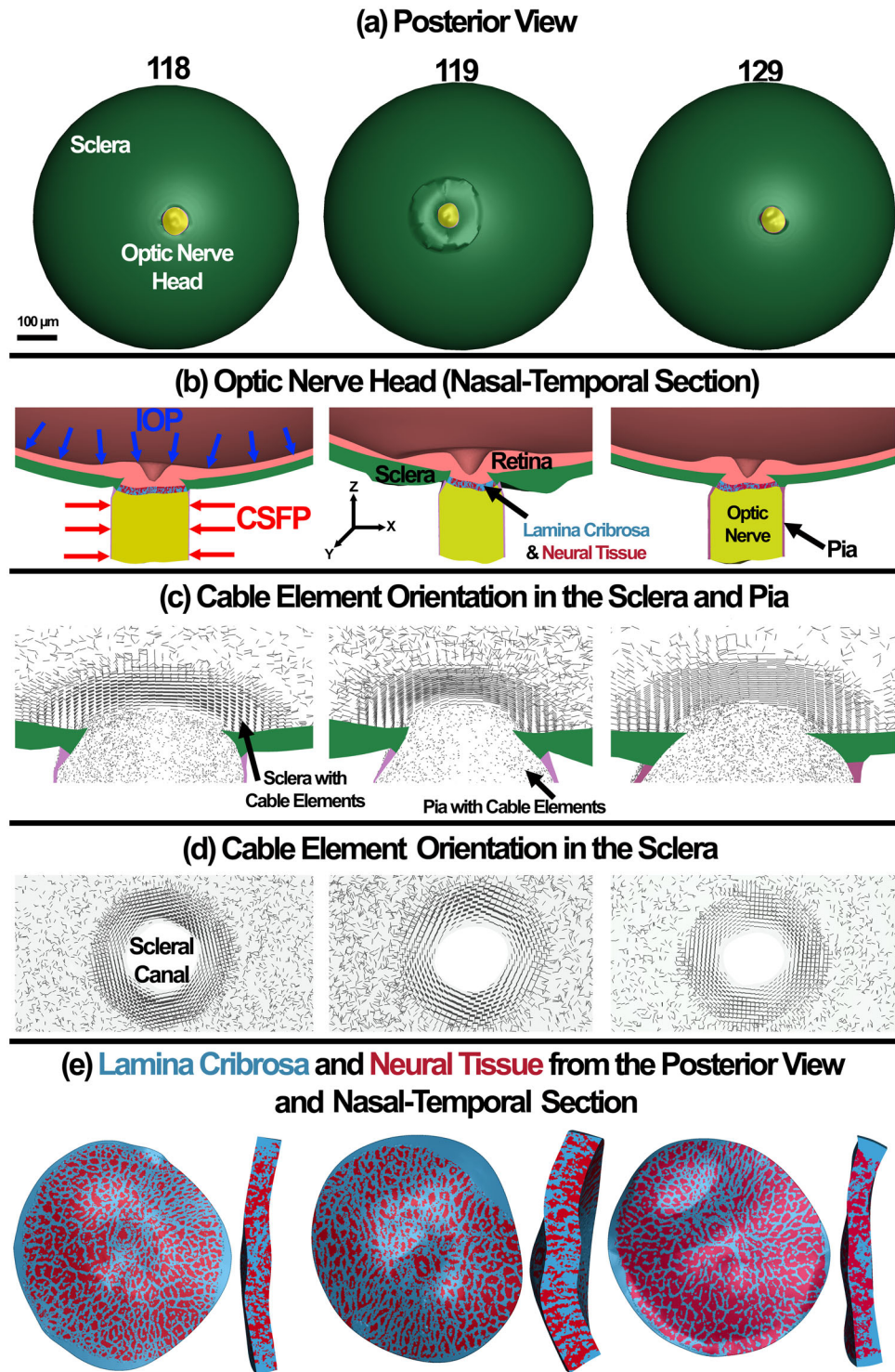


FIGURE 1. Details of the eye models from human donors 118, 119, 129 showing (a) posterior view of the model, (b) nasal-temporal section of the posterior eye FE model through the ONH, (c) directional distribution of the embedded cable elements representing the inhomogeneous anisotropic collagen fibril orientation in the sclera (circumferential, radial, and planar isotropic) and pia (planar isotropic), (d) top view of the cable element orientation in the sclera only, and (e) close-up views of the lamina cribrosa and laminar neural tissue microstructural FE models.

matrix of the connective tissues was modeled as hyperelastic neo-Hookean material, whereas the cable elements that represent the directional stiffness imparted by anisotropic collagen fibril orientation were modeled as elastic material.

A custom MatLab script was used to detect the load surface, equivalence the nodes at the components' interfaces, define the materials' sections, define the element sets, and write the final LS-Dyna (Ansys/LS-DYNA, Canonsburg, PA, USA)

TABLE 1. The Material Parameters of the Eye-Specific FE Models of Donors 118, 119, and 129

Tissue	Shear Modulus, μ (MPa)	Elastic Modulus, E (MPa)	Density, ρ (kg/m ³)
Retina ⁶²	0.01	–	1100
Sclera ⁶²	1.64	–	1243
Lamina cribrosa ⁶²	0.40	–	1243
Neural tissue ⁶²	0.01	–	1100
Pia ⁶²	1.64	–	1100
Optic nerve ⁶²	0.01	–	1100
Sclera fibers ⁶⁹	–	600	1100
Pia fibers ⁶⁹	–	600	1100

The bulk modulus was set to $\kappa = 100 \mu$, where $\mu =$ shear modulus for all tissues.^{62,69} The solid matrix was modeled as a neo-Hookean hyperelastic material model and the directional stiffness imparted by anisotropic collagen fibers were simulated using discrete cable elements embedded in the solid matrix. The scleral solid matrix and cable element properties were fit from experimental data, and the lamina cribrosa properties were fit from experimental displacement data as specified in the referenced study.⁶⁹ The pia mater matrix and cable element properties were assumed to be the same as the sclera, as they have similar composition. The neural tissues were assumed to be a very soft, nearly incompressible solid as is done in most ONH biomechanics studies.⁶²

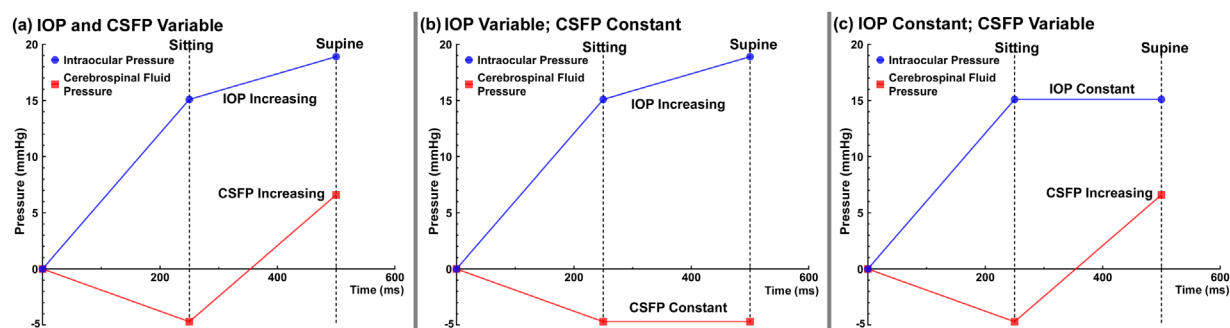


FIGURE 2. Dynamic time course of the IOP and CSFP load cases applied to the eye FE models, representing the sitting (0 to 250 ms) and supine body positions (250 to 500 ms), including (a) IOP and CSFP variable, (b) IOP variable; CSFP constant, and (c) IOP constant; CSFP variable. Note that these load cases were designed to isolate the relative independent contributions of IOP and CSFP to TLP change with postural transition.

input file.^{64,74} The final FE models from donors 118, 119, and 129 consist of 3,462,772/3,813,732; 2,488,608/2,749,153; and 3,079,555/3,418,278 elements/nodes, respectively, with a minimum and maximum element edge lengths in the LC and NT of 5 and 12 μ m, respectively. To assess scleral canal deformations, a custom MatLab script was written to calculate the diameters of the anterior scleral canal opening (ASCO), posterior scleral canal opening (PSCO), anterior lamellar insertion (ALI), and posterior lamellar insertion (PLI) based on nodal deformation, as described previously.⁶³ To evaluate the effects of the mesh density on the results, the models were simulated and the results compared in terms of the average radial displacement of the scleral canal at the ALI, PLI, and PSCO, average depth of the anterior lamellar surface, volumetric average first principal strain in the LC, and maximum von Mises stress in the LC, as described in our recent publication.⁶⁴ The models, assessed in terms of the resultant stresses and strains, as well as the radial expansion of the scleral canal, were all converged as explained in our prior publication.⁶⁴

To prevent rigid body motion of the FE models, the nodes of the sclera and retina along the cut face of the globe at the equator were selected and constrained to $Z = \text{constant}$ ($U_x = U_y = U_R = 0$), which permits only radial displacement (globe expansion) in the equatorial plane. IOP and CSFP load boundaries were applied on the inner surface of the retina and outer surface of the pia, respectively. To isolate the

roles of IOP and/or CSFP elevations on the resultant stresses and strains in the LC beams and NT, three different load cases were specified: (1) IOP ($\uparrow 3.8$ mm Hg) and CSFP ($\uparrow 11.3$ mm Hg) variable, (2) IOP variable ($\uparrow 3.8$ mm Hg); CSFP constant (-4.7 mm Hg), and (3) IOP constant (15.1 mm Hg); CSFP variable ($\uparrow 11.3$ mm Hg; Fig. 2). The pressures were applied in two continuous steps from zero load to the sitting position (0 to 250 ms) and from sitting to the supine position (250 to 500 ms).⁴⁰ A computer with a 10-core Intel Xeon CPU running at 3.30 GHz with 256 GB RAM was used to run the simulations in LS-DYNA. The simulation was conducted with quasi-static IOP and CSFP change occurring over 500 ms in total, with a time step of 10 ms (50 time steps) using the Implicit solver. This loading time and rate is typical of the time required to move from the sitting to supine positions, and is well within the physiologic range.^{41,75} The simulations for donors 118, 119, and 129 took 51, 38, and 45 hours, respectively, to run on our workstation.

Statistical Analysis

The resultant stresses and strains, including the first principal, third principal, and maximum shear, from the simulation of three eye-specific FE models were determined to be normally distributed using descriptive statistics module in IBM SPSS (IBM, Armonk, NY, USA). The statistical significance of the difference between model results were

evaluated using a randomized 1-way analysis of variance (ANOVA). When indicated by a significant F statistic after a 1-way ANOVA, post hoc comparisons with the Scheffe method⁷⁶ were used to determine the individual levels of significant differences among the resultant stresses, strains, and deformations under different combinations of IOP and CSFP loading conditions. The criterion chosen to discard the null hypothesis was $P < 0.05$.

RESULTS

The first principal stresses and strains in the ONH FE models in the sitting and supine body postures are shown in Figure 3 for the nasal-temporal cross section through the ONH. The first principal stresses and strains in the LC beams only, and laminar NT only, are shown in Figure 4 for the sitting and supine positions. The movies showing the progression in the first principal strain in both the nasal-temporal section through the ONH and posterior laminar surface, as donor 118 transitions from the sitting to supine position, are attached as Movie 1 and Movie 2.

The third principal stresses and strains in the ONH FE models in the sitting and supine body postures are shown in Supplementary Figure S1 for the nasal-temporal cross section. The third principal stresses and strains in the LC beams only, and laminar NT only, are shown in Supplementary Figure S2 for the sitting and supine positions. The maximum shear stresses and strains in the ONH FE models in the sitting and supine body postures are shown in Supplementary Figure S3 for the nasal-temporal cross section. The maximum shear principal stresses and strains in the LC beams only, and laminar NT only, are shown in Supplementary Figure S4 for the sitting and supine positions.

The anterior and posterior views of the axial force in the circumferential, radial, and planar isotropic cable elements embedded in the peripapillary sclera in the sitting and supine positions are shown in Figure 5.

Figure 6 shows the contour maps of the tissue pressure in the nasal-temporal cross section through the ONH in 2 eye models from donor 118, for which CSFP in the sitting position was assigned as either -4.7 mm Hg⁴⁰ or $+2$ mm Hg.³⁰ Volumetric average pressures for the LC beams and laminar NT are shown for both CSFP boundary conditions.

The volumetric average first principal, third principal, and maximum shear stresses and strains in the LC beam, NT, and peripapillary sclera, as well as average axial force in the peripapillary scleral cable elements that represent the collagen fibers, are summarized in Table 2 for a postural change from sitting to supine. The volumetric average first principal and maximum shear stresses and strains in the LC beam, NT, and PPScl due to change in body posture, normalized per mm Hg in TLP, IOP, or CSFP change, are summarized in Table 3 for a postural change from sitting to supine. In addition, the average IOP- and CSFP-driven radial expansion of the scleral canal at the ASCO, PSCO, ALI, and PLI, as well as the average and maximum anterior laminar surface depth, is reported in Table 4 for a postural change from sitting to supine. Finally, the average IOP- and CSFP-driven radial expansion in the ASCO, PSCO, ALI, and PLI, as well as the average and maximum anterior laminar surface depth (ALSD), normalized per mm Hg change in TLP, IOP, and CSFP, are listed in Table 5 for a postural change from sitting to supine.

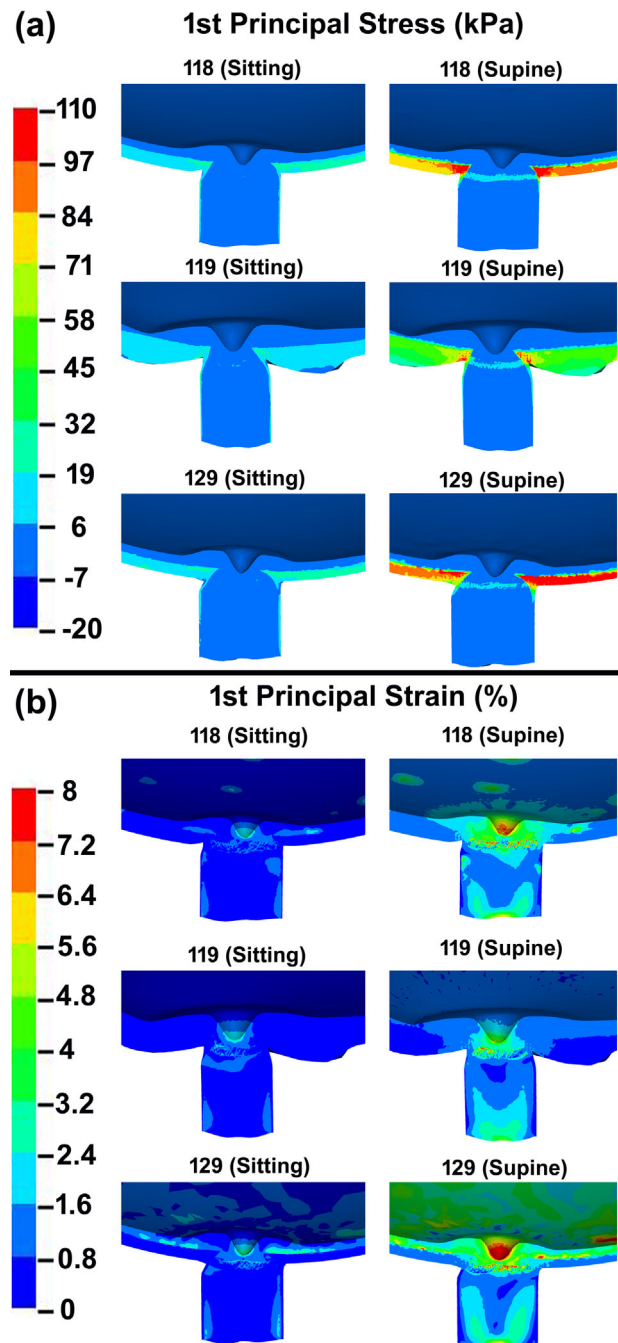


FIGURE 3. Contour maps of the first principal (tensile). (a) Stress and (b) strain in the eye FE models in the sitting and supine body positions are shown for the nasal-temporal section.

DISCUSSION

An increased TLP, whether due to decreased CSFP,^{9,10,12,14} increased IOP,^{12,77} or a combination of both, may be important in primary open-angle glaucoma, especially when it occurs at IOPs that are in the normal range. Several studies have suggested that TLP alteration is potentially a greater risk factor for glaucoma than elevated IOP alone.^{9,10,12–14,78,79} Whereas IOP and CSFP may have direct effects on cells, they are mechanical pressures, and so understanding the role of the TLP change in ONH biomechanics

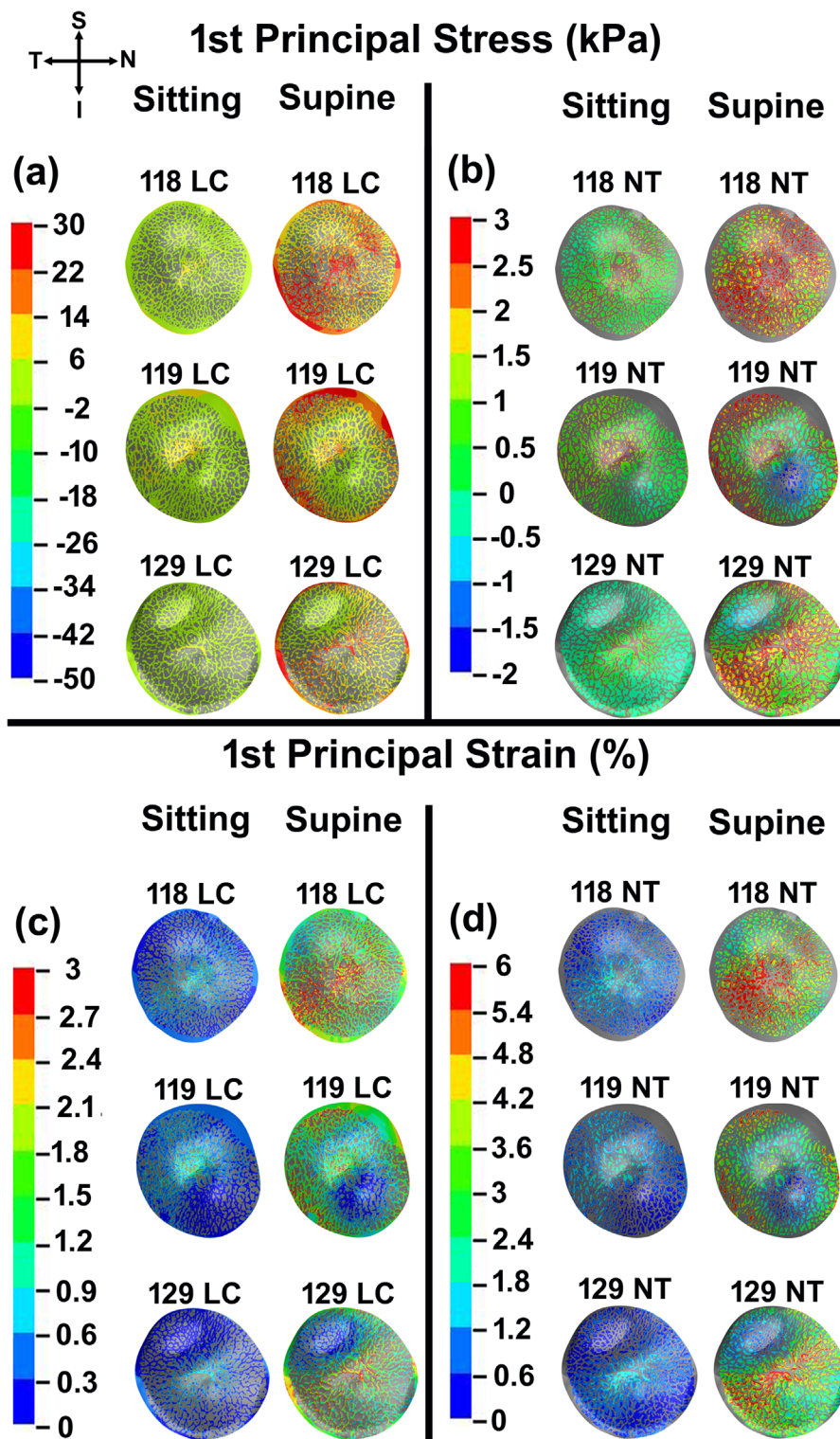


FIGURE 4. Contour maps of the first principal (tensile) stress in the (a) LC only and (b) NT only, as well as contour maps of the first principal strain in the (c) LC only and (d) NT only, in the sitting and supine body positions for all three human eye models.

may help determine if specific patients are more vulnerable to glaucomatous damage or are likely to progress more rapidly. Better understanding of the TLP-driven stresses and strains in the ONH connective and neural tissues may contribute to developing more effective treatments.⁸⁰

However, experimental imaging studies have been unable to provide comprehensive stress and strain estimation for the LC beam and laminar NT microstructures due to insufficient imaging resolution, limited penetration depth, and shadowing by overlying blood vessels and pigmented

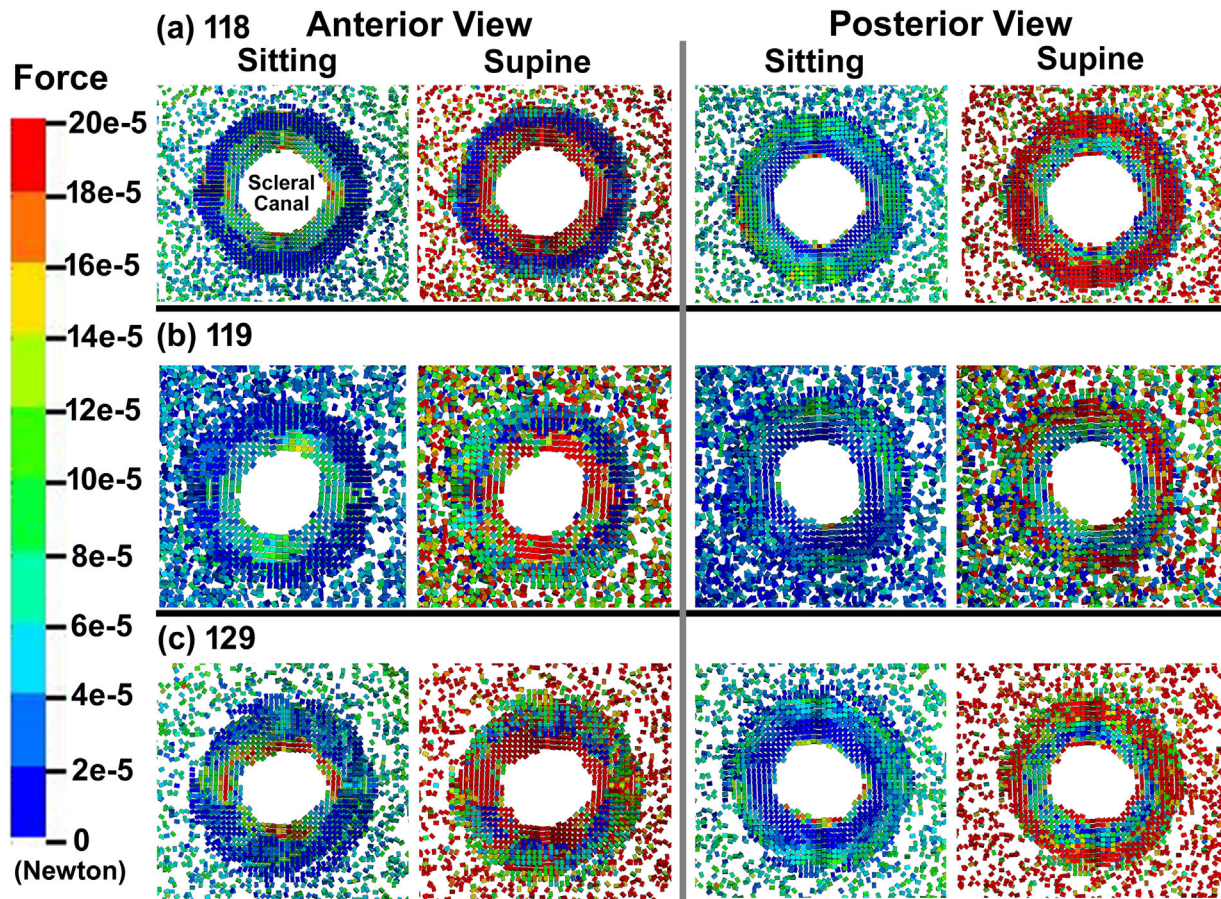


FIGURE 5. Anterior and posterior views of the axial force in the peripapillary scleral cable elements that represent the anisotropic collagen fiber stiffness in the sitting and supine body positions for the eye models of human eye donors (a) 118, (b) 119, and (c) 129.

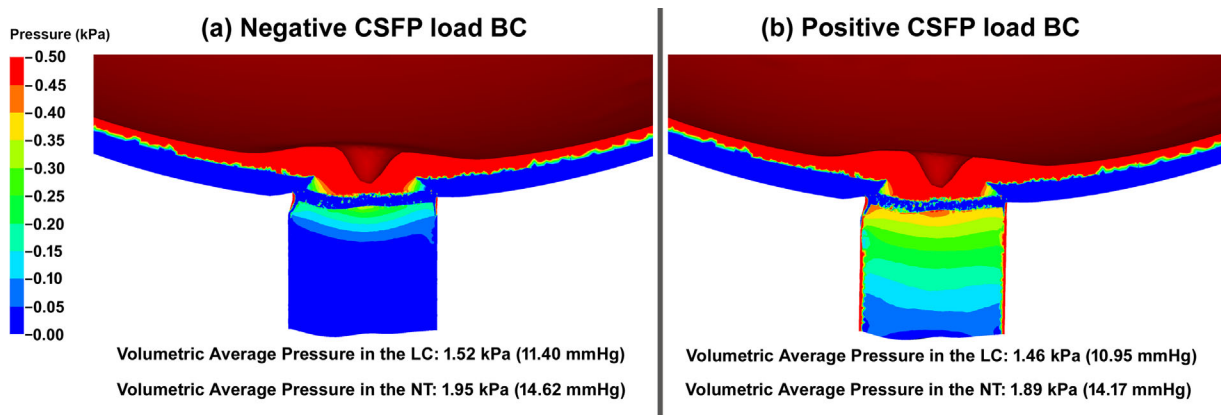


FIGURE 6. Contour maps of pressure in the donor 118 FE model in sitting body position for the nasal-temporal section under (a) negative 4.7 mm Hg CSFP and (b) positive 2 mm Hg CSFP load boundary conditions (BCs).

membranes.^{81,82} Computational simulations can fill that gap by estimating the full 3D biomechanical response of the ONH and the laminar connective and neural tissue microstructures. Herein, we constructed three eye-specific FE models that included both the full LC beam and NT microstructures,⁶² as well as cable elements that represent the directional stiffness imparted by anisotropic collagen fibers in the peripapillary sclera and pia⁶³ (see Fig. 1). Three

different load cases representing a postural change from sitting to supine were applied to the models as (1) IOP and CSFP variable (physiologic), (2) IOP variable; CSFP constant, and (3) IOP constant; CSFP variable (see Fig. 2) to calculate the relative independent contributions of IOP and CSFP to the biomechanical response of the ONH.

In all three donor eye models, tensile and shear stresses and all strain components were significantly increased in all

TABLE 2. Volumetric Average Stresses and Strains in the Lamina Cribrosa (LC), Laminae Neural Tissue (NT), Peripapillary Sclera (PPScl), and the Average Axial Force in the Cable Elements in the PPScl Region Due to Change in Body Posture

Simulations	Tissues	First Principal Stress (kPa)	First Principal Strain (%)	Third Principal Stress (kPa)	Third Principal Strain (%)	Max Shear Stress (kPa)	Max Shear Strain (%)	Axial Force (N)
118-IOP and CSFP variable	LC	6.97	0.58	-2.60	-0.61	4.79	0.59	-
	NT	1.75	2.27	0.79	-2.59	0.48	2.43	-
	LC + NT	4.42	1.47	-1.59	-1.55	2.52	1.70	-
	PPScl	39.44	0.72	-3.61	-0.58	21.53	0.65	-
118-IOP variable; CSFP constant	Cable element	-	-	-	-	-	-	16.40e-5
	LC	8.21	0.65	-2.41	-0.67	5.31	0.66	-
	NT	2.29	2.50	1.23	-2.83	0.53	2.67	-
	LC + NT	5.11	1.48	-1.29	-1.65	2.88	1.55	-
118-IOP constant; CSFP variable	PPScl	40.62	0.75	-3.34	-0.58	21.98	0.67	-
	Cable Element	-	-	-	-	-	-	16.67e-5
	LC	6.65	0.55	-2.38	-0.57	4.52	0.56	-
	NT	1.73	2.15	0.82	-2.44	0.45	2.30	-
119-IOP and CSFP variable	LC + NT	4.12	1.29	-1.52	-1.44	2.38	1.49	-
	PPScl	37.35	0.68	-3.20	-0.55	20.27	0.61	-
	Cable element	-	-	-	-	-	-	15.13e-5
	LC	5.00	0.43	-1.99	-0.44	3.50	0.43	-
119-IOP variable; CSFP constant	NT	0.99	1.46	0.40	-1.59	0.29	1.49	-
	LC + NT	2.88	0.95	-1.09	-0.92	1.74	1.04	-
	PPScl	28.28	0.50	-2.75	-0.44	15.53	0.47	-
	Cable element	-	-	-	-	-	-	8.89e-5
119-IOP constant; CSFP variable	LC	6.65	0.49	-1.41	-0.51	4.03	0.51	-
	NT	1.91	1.70	1.20	-1.89	0.35	1.79	-
	LC + NT	4.29	1.08	-1.10	-1.18	2.15	1.11	-
	PPScl	28.64	0.51	-2.62	-0.44	15.63	0.47	-
129-IOP and CSFP variable	Cable element	-	-	-	-	-	-	8.92e-5
	LC	4.6	0.39	-1.82	-0.40	3.21	0.40	-
	NT	0.94	1.29	0.40	-1.45	0.27	1.37	-
	LC + NT	2.78	0.86	-1.06	-0.95	1.69	0.95	-
129-IOP variable; CSFP constant	PPScl	26.39	0.46	-2.45	-0.40	14.42	0.43	-
	Cable element	-	-	-	-	-	-	8.01e-5
	LC	6.68	0.53	-1.75	-0.51	4.21	0.52	-
	NT	1.32	1.82	0.55	-2.02	0.38	1.92	-
129-IOP constant; CSFP variable	LC + NT	3.88	1.05	-1.03	-1.31	2.32	1.26	-
	PPScl	37.99	0.70	-3.13	-0.54	20.56	0.62	-
	Cable element	-	-	-	-	-	-	14.95e-5
	LC	7.62	0.57	-1.40	-0.54	4.51	0.56	-
129-IOP variable; CSFP constant	NT	1.84	2.02	1.00	-2.20	0.41	2.11	-
	LC + NT	4.66	1.12	-0.81	-1.21	2.23	1.20	-
	PPScl	39.08	0.73	-3.12	-0.54	21.10	0.63	-
	Cable element	-	-	-	-	-	-	15.19e-5
129-IOP constant; CSFP variable	LC	6.42	0.51	-1.55	-0.48	3.99	0.49	-
	NT	1.34	1.73	0.62	-1.91	0.36	1.82	-
	LC + NT	3.77	1.15	-0.98	-1.05	2.09	1.16	-
	PPScl	36.27	0.67	-2.64	-0.51	19.45	0.59	-
	Cable element	-	-	-	-	-	-	13.85e-5

All values of the first principal stress, max shear stress, and all values of strain were statistically different from sitting ($P < 0.05$), indicative of significant change with body position.

tissues when transitioning from the sitting to supine body positions ($P < 0.05$; see [Tables 2, 3](#); [Figs. 3, 4](#)). Compressive stress in the laminae NT and PPScl also followed this trend, and the lone exception to this finding was the compressive stress in the LC beams and LC + NT together, which was larger with CSFP change than IOP change. Compressive stress could be affected by the initial loading of nega-

tive 4.7 mm Hg CSFP in the sitting position, which transitions to positive 6.6 mm Hg CSFP in the supine position.⁴⁰ One may assume that a negative CSFP would affect the retrolaminar tissue pressure, but our simulations estimate that retrolaminar tissue pressure is positive even when CSFP in the adjacent subarachnoid space is negative (see [Fig. 6](#)). To investigate this further, we changed the sitting CSFP to

TABLE 3. Volumetric Average Stresses and Strains in the Lamina Cribrosa (LC), Neural Tissue (NT), and Peripapillary Sclera (PPScl) Due to Change in Body Posture, Normalized Per mmHg of IOP, CSFP and TLP Change

Simulations	Tissues	First Principal Stress (kPa/mm Hg)	First Principal Strain (%/mm Hg)	Max Shear Stress (kPa/mm Hg)	Max Shear Strain (%/mm Hg)
118-IOP and CSFP variable	LC	0.92	0.07	0.63	0.07
	NT	0.23	0.30	0.06	0.32
	LC + NT	0.58	0.19	0.33	0.22
	PPScl	5.25	0.09	2.87	0.08
118-IOP variable; CSFP constant	LC	2.16	0.17	1.39	0.17
	NT	0.60	0.65	0.13	0.70
	LC + NT	1.34	0.38	0.75	0.40
	PPScl	10.68	0.19	5.78	0.17
118-IOP constant; CSFP variable	LC	0.58	0.04	0.40	0.04
	NT	0.15	0.19	0.03	0.20
	LC + NT	0.36	0.11	0.21	0.13
	PPScl	3.30	0.06	1.79	0.05
119-IOP and CSFP variable	LC	0.66	0.05	0.46	0.05
	NT	0.13	0.19	0.03	0.19
	LC + NT	0.38	0.12	0.23	0.13
	PPScl	3.77	0.06	2.07	0.06
119-IOP variable; CSFP constant	LC	1.75	0.12	1.06	0.13
	NT	0.50	0.44	0.09	0.47
	LC + NT	1.127	0.28	0.56	0.29
	PPScl	7.53	0.13	4.11	0.12
119-IOP constant; CSFP variable	LC	0.40	0.03	0.28	0.03
	NT	0.08	0.11	0.02	0.12
	LC + NT	0.24	0.07	0.14	0.08
	PPScl	2.33	0.04	1.27	0.03
129-IOP and CSFP variable	LC	0.89	0.07	0.56	0.06
	NT	0.17	0.24	0.05	0.25
	LC + NT	0.51	0.14	0.30	0.16
	PPScl	5.06	0.09	2.74	0.082
129-IOP variable; CSFP constant	LC	2.00	0.15	1.18	0.14
	NT	0.48	0.53	0.10	0.55
	LC + NT	1.22	0.29	0.58	0.31
	PPScl	10.28	0.19	5.55	0.16
129-IOP constant; CSFP variable	LC	0.56	0.04	0.35	0.04
	NT	0.11	0.15	0.03	0.16
	LC + NT	0.33	0.10	0.18	0.10
	PPScl	3.20	0.05	1.72	0.05

All values were statistically different from sitting ($P < 0.05$), indicative of significant change with body position.

TABLE 4. Average Radial Expansion of the Scleral Canal at the Anterior Scleral Canal Opening (ASCO), Posterior Scleral Canal Opening (PSCO), Anterior Lamina Insertion (ALI), and Posterior Lamina Insertion (PLI), Along With the Average and Maximum Anterior Lamina Surface Depth (ALSD) Due to IOP, CSFP, and TLP Change With Transition From the Sitting to Supine Body Position

Simulations	ASCO (µm)	PSCO (µm)	ALI (µm)	PLI (µm)	Average ALSD (µm)	Max ALSD (µm)
118-IOP and CSFP variable	22	18	18	11	2	6
118-IOP variable; CSFP constant	19	21	17	20	3	8
118-IOP constant; CSFP variable	21	17	16	14	3	6
119-IOP and CSFP variable	10	7	10	7	5	13
119-IOP variable; CSFP constant	9	8	10	8	2	7
119-IOP constant; CSFP variable	9	7	9	7	5	12
129-IOP and CSFP variable	20	12	17	12	7	15
129-IOP variable; CSFP constant	19	13	17	13	3	11
129-IOP constant; CSFP variable	19	11	16	11	6	14

+2 mm Hg, an alternative condition supported by experimental measurements in the dog,^{23,30} which also resulted in a positive retrolaminar neural tissue pressure that was not substantially different from the negative CSFP loading case, and had negligible effects on the LC and NT tissue pressures (see Fig. 6).

In general, the highest strains, the physical manifestation of stress, in the LC beams and lamina NT were observed in the inferotemporal sector, where damage to the retinal ganglion cell axons is known to be most prominent in glaucoma⁸⁵ (see Figs. 4, Supplementary Figs. S2, S4). Shear strains were also found to be larger in the peripheral lamina

TABLE 5. Average Radial Expansion of the Scleral Canal at the Anterior Scleral Canal Opening (ASCO), Posterior Scleral Canal Opening (PSCO), Anterior Lamina Inset (ALI), and Posterior Lamina Inset (PLI), Along With the Average and Maximum Anterior Lamina Surface Depth (ALSD) Due to IOP, CSFP, and TLP Change With Transition From the Sitting to Supine Body Position

Simulations	ASCO ($\mu\text{m}/\text{mm Hg}$)	PSCO ($\mu\text{m}/\text{mm Hg}$)	ALI ($\mu\text{m}/\text{mm Hg}$)	PLI ($\mu\text{m}/\text{mm Hg}$)	Average ALSD ($\mu\text{m}/\text{mm Hg}$)	Max ALSD ($\mu\text{m}/\text{mm Hg}$)
118-IOP and CSFP variable	2.93	2.40	2.40	1.46	0.26	0.80
118-IOP variable; CSFP constant	5	5.52	4.47	5.26	0.78	2.10
118-IOP constant; CSFP variable	1.85	1.50	1.41	1.23	0.26	0.53
119-IOP and CSFP variable	1.33	0.93	1.33	0.93	0.67	1.73
119-IOP variable; CSFP constant	2.36	2.10	2.63	2.10	0.52	1.84
119-IOP constant; CSFP variable	0.79	0.62	0.79	0.62	0.44	1.06
129-IOP and CSFP variable	2.67	1.60	2.26	1.60	0.93	2
129-IOP variable; CSFP constant	5	3.42	4.47	3.42	0.78	2.89
129-IOP constant; CSFP variable	1.68	0.97	1.41	0.97	0.53	1.23

compared to the center,⁸⁴ and the maximum shear strain was the highest at the boundary with the considerably stiffer sclera.⁸⁵ Herein, a larger shear strain was observed in the peripheral regions compared to the central region, and the shear strain was the highest in the peripheral lamina of donor eye 119 that had the thickest PPScl compared with donors 118 and 129. Moreover, our models showed a lower shear strain in the PPScl compared to the central LC regions (see Supplementary Fig. S3) that is in good agreement with Midgett et al.⁸⁴

Tensile (first principal), compressive (third principal), and maximum shear stresses and strains showed interesting patterns with the three loading cases, which, again, were designed to separate out the relative independent contributions of IOP and CSFP change to TLP-driven biomechanical effects with the transition from the sitting to supine position. In all simulations (IOP increase alone, CSFP increase alone, and both IOP and CSFP increase simultaneously; see Fig. 2) all components of stress and strain were greater in the LC beam, lamina NT, and PPScl in the supine position compared to the sitting position (see Table 2). With body position change from sitting to supine, the LC beams in all three models showed three to five times greater stress and three to five times lower strain than the interspersed lamina NT, which exhibited much lower stresses and higher tensile strains. This result illustrates the important structural role of the LC beams in protecting the delicate retinal ganglion cells axons that weave through the LC pores in the lamina region.⁶² It also shows the relatively high strains in the lamina NT, which may be important in glaucoma pathogenesis and progression.

Keeping in mind that CSFP provides a counterpressure to IOP, but only at the ONH itself, interesting patterns emerge when comparing the stress and strain in the ONH tissues across the three load cases. Interestingly, although IOP changed less (3.8 mm Hg) with body position than CSFP (11.3 mm Hg), it had a larger effect on lamina tissue (LC, NT, and LC + NT) stress and strain than CSFP. This is likely due to the scleral canal expansion associated with IOP change, which also affects the lamina tissues because they are inserted into the scleral canal wall and therefore stretch/relax when the canal expands/contracts.^{20,86} This is the case in these simulations as shown in Table 4, wherein the scleral canal expansion at the ALI and PLI into the scleral canal wall were larger with IOP change, which acts on the full scleral shell, compared to CSFP change alone, which acts primarily on the lamina tissues, even though the CSFP change is much larger.

Although TLP = IOP-CSFP, it is clear from the data presented in Tables 2 and 4 that the effects of IOP and CSFP are not similar or additive in terms of their effects on the stress, strain, and deformations of the ONH tissues. IOP changes much less than CSFP with postural transition from sitting to supine, but IOP drives a larger biomechanical change in all parameters and all tissues compared to CSFP. To quantify these pressure effects more clearly, stresses, strains, and deformations were normalized per mm Hg change in IOP and CSFP in Tables 3 and 5. This approach shows that IOP drives stress, strain and deformation in the ONH tissues at two to four times the rate of CSFP per mm Hg when both are changing simultaneously with postural transition. This is an important result, as it shows that whereas CSFP should provide a direct, one-to-one counterpressure to IOP at the ONH and across the LC, it is much less impactful than the TLP equation above would suggest. This result is in line with the findings of computational studies by Hua and Mao, who used simplified axisymmetric parametric models with homogenous, elastic material properties to show that IOP had a larger effect (approximately 2 times) per mm Hg than CSFP on stress and strain in homogenized lamina tissues (LC + NT considered as one bulk material).^{53,87} Results presented herein extend those findings to the PPScl and the LC beams and lamina NT microstructures, in eye-specific models with realistic geometries and inhomogeneous, anisotropic, hyperelastic material properties that can better mimic in vivo behavior. Further, our models predict that the IOP effects are up to four-fold larger per mm Hg than CSFP, which is approximately double that predicted by prior studies.

Most clinical and experimental studies assessing ONH biomechanics in vivo with optical coherence tomography (OCT) imaging use Bruch's Membrane opening (BMO) as the reference for LC position measurements with OCT because it is readily visible in OCT images and the scleral canal is often shadowed by overlying structures.⁸⁸ Bruch's Membrane is not present in our models, and so we used the ALI as the reference for LC position calculation in this study. Slight changes in the anterior-to-posterior position of BMO with IOP or CSFP change could affect our ability to make direct comparisons between the modeling results herein to prior work. In addition, there have been several studies that report the LC and PPScl strains with IOP, CSFP or TLP change quantified using OCT imaging methods, which are directly compared with our modeling results below, with some caveats. Note that visibility of the PPScl, scleral canal wall, peripheral/posterior LC, and retrolamina optic nerve with

OCT is both difficult and eye specific due to image attenuation with depth and shadowing by overlying structures, so the most valid comparisons are with central LC strains. In addition, *in vivo* strain imaging studies cannot distinguish between the LC and NT microstructures, so results should be compared to the LC + NT strains listed in [Tables 3 and 4](#).

Prior studies have assessed the stress, strain, and deformation of the ONH with IOP and CSFP change. Fazio and co-workers measured maximum shear strain in the ONH of a single glaucoma eye in a living brain-dead organ donor via OCT, and reported IOP-driven strain change as 0.06%/mm Hg in the LC and 0.16%/mm Hg in the PPScl, respectively.⁴⁸ CSFP-driven shear strain change was reported as -0.14%/mm Hg globally for a *decrease* in CSFP (supine to sitting).⁴⁸ Our modeling results yielded an average IOP-driven shear strain change of 0.33%/mm Hg in the LC and 0.15%/mm Hg for the PPScl, and the CSFP-driven shear strain change as 0.10%/mm Hg for the LC and 0.04%/mm Hg for an *increase* in CSFP. Although our simulation results match the IOP-related shear strain change the PPScl, our estimates of LC strains were much higher than the Fazio study.⁴⁸ This could be due to much greater backpressure against IOP acting through a cupped and remodeling glaucomatous LC in the Fazio study, both of which may have affected their results. CSFP was estimated at 14 and 24 mm Hg in the sitting and supine positions, respectively, due to brain damage in the donor, which is much larger than the -4.7 mm Hg we assumed in the models for the sitting position. In addition, their *in vivo* strain measurements were taken in a single glaucoma eye, which have much different biomechanical behavior and morphology than healthy controls. Girard and colleagues reported that glaucoma eyes exhibited approximately eight times greater LC strain relief than healthy controls after IOP lowering in an OCT-based *in vivo* strain study.⁵⁶ However, this study did not evaluate the impact of CSFP on LC strain. They also reported relatively small strain decreases in the laminar region and PPScl after IOP lowering in healthy controls that were similar in magnitude to our results.

Prior studies have also assessed the stress, strain, and deformation of the ONH with TLP change (simultaneous IOP and CSFP elevation). Valsalva is known to increase both IOP by approximately 5 mm Hg in upright normal patients^{89,90} and CSFP by approximately 10.5 mm Hg in neurological patients in the lateral decubitus position⁸⁹; these pressure changes are very similar to the IOP and CSFP increases associated with transition from a sitting to supine position used in this study. Kim colleagues assessed maximum LC displacement (equivalent to Max ALSD in [Tables 4 and 5](#)) via OCT imaging in human patients before and during Valsalva maneuver.⁹⁰ In young patients less than 50 years old, Max ALSD decreased (LC moved anteriorly) significantly by approximately 35 μ m, but only slight non-significant changes (-5 to +3 μ m) were seen in older patients like those used in this study, in which our models also predicted similar, small maximum LC deformations of 6 to 15 μ m. Note that IOP change was slightly smaller with the postural change modeled herein (3.9 mm Hg) compared with Valsalva (approximately 5 mm Hg), which could explain this slight discrepancy since IOP elevation tends to increase scleral canal diameter and hence pulls the LC taut (anteriorly).⁸⁶ Moreover, a study by Kedar and co-workers⁹¹ in both human subjects and pigs, failed to detect any change in LC position via OCT with even relatively large changes in CSFP (3–26 mm Hg in humans and 5–35 mm Hg in pigs), suggesting

that both LC deformation and strains are small in response to CSFP change. Laminar deformations can be difficult to discern with OCT due to limited axial resolution, and there was a large variability in the LC response to CSFP perturbation in this study (see [figure 3](#) in [Ref. 91](#)).

Several groups have reported ONH strain and deformations with IOP and CSFP manipulation in more invasive studies that can be done in animal models. In a particularly relevant study, Zhu and co-workers reported the LC deformation in NHPs subjected to independent manometric manipulation of IOP and CSFP.⁹² They reported that CSFP elevation displaced the LC anteriorly by 10 μ m at baseline IOP but the LC displaced 7 μ m posteriorly at high IOP; these results are somewhat counterintuitive, although the relatively small changes were of the same magnitude as those we report herein. Similar magnitude LC deformations results were reported for IOP elevations at baseline and elevated CSFP. The discrepancy between our results, which show that both IOP and CSFP elevations induce small posterior LC deformations, may be due to the large CSFP (10–40 mm Hg) and IOP (10–50) elevations used in the NHP study, which are much larger than the relatively small, low-level changes in IOP and CSFP we used herein. In addition, results could be affected by the more structurally compliant sclera in the NHP, which is much thinner^{93,94} and more compliant compared to human sclera.⁹⁵ Recall that a more compliant PPScl, such as NHPs, tends to affect LC displacement to a greater degree through scleral canal expansion than in eyes with stiffer sclera (human), although other factors are at play.⁸⁶ In our simulations, donor eye 119 had a much thicker sclera, and exhibited scleral canal expansion with IOP and CSFP elevation that was only approximately 50% as large as that estimated for donors 118 and 129, although LC deformations were similar in all donor eye models. Our models predict that CSFP elevation results in PPScl and LC + NT tensile strains of 0.6% and 1.1% with posture change (see [Table 2](#)), respectively, which is in good agreement with that of 0.5–1% and 1–1.5% strains for the PPScl and LC reported by Feola et al. in enucleated pig eyes subjected to IOP and CSFP elevations.⁴⁹

Computational studies have shown that the direction and magnitude of LC displacement are significantly influenced by the mechanical response of the sclera,^{47,96} with a stiffer sclera causing less canal expansion and more posterior deformation in the LC, although this basic relation can be complex and dependent on other factors.⁸⁶ In this study, the sclera in all three FE models were assigned the same mechanical properties for the solid matrix and the embedded cable elements (see [Table 1](#)) with the only difference being the scleral geometry. The cable elements representing the collagen fibers exhibited greater axial force in the supine position compared to the sitting body position (see [Supplementary Fig. S4](#)). The highest axial force occurred when only IOP was varied, whereas the lowest axial force when only CSFP was varied (see [Table 2](#)), indicating that IOP affects the PPScl much more than CSFP as seen in prior studies. In all three donor eye models, scleral canal expansion and change in ALSD were driven primarily by IOP elevation rather than CSFP change ($P < 0.05$; see [Tables 4, 5](#)), which is in good agreement with Feola et al.⁵² Model 119 due to a thicker PPScl showed a lower canal expansion (see [Tables 4, 5](#)). ALSD is one of the key biomarkers of glaucomatous optic neuropathy⁹⁷ because experimental studies have shown that LC displacement occurs at an early stage of the disease,^{98,99} and may precede the retinal nerve fiber

layer change as detected by OCT.¹⁰⁰ CSFP and IOP elevation increased the average and maximum ALSD by 4.67 μm and 11.30 μm , respectively, that is in good agreement with *in vivo* measurements in monkeys (7 μm).⁵⁴

Retrolaminar CSFP is not known for humans in the sitting position, and there is some disagreement in the literature; published values range from 4.4 mm Hg^{17,101,102} to -4.7 mm Hg, derived from calculated measures based on either intracranial pressure or CSFP in the lumbar spine.⁴⁰ To complicate matters further, direct retrolaminar pressure measurements in dogs suggest that while intracranial CSFP (ICP) can be negative as the Eklund study estimates,⁴⁰ the actual retrolaminar CSFP cannot fall below the orbital tissue pressure of 0 to 2 mm Hg because the dural sheath around the optic nerve is not rigid and hence cannot sustain a negative pressure.³⁰ To assess the possibility that our results could be affected by positive or negative CSFP loading at the sitting position, the volumetric average pressures in the LC and NT were calculated for CSFP loadings of -4.7 and 2 mm Hg in the sitting position in donor 118. The results of this simulation are plotted in Figure 6, which shows that retrolaminar tissue pressure remains positive immediately posterior to the LC in both cases, and LC and NT pressures are unaffected by positive or negative CSFP load boundary. Future studies will investigate the effects of the optic nerve loading and boundary conditions, which prior studies have suggested is important in modeling the ONH biomechanical response.⁵³

Limitations

This study is limited by the following considerations. First, there is no validated gold standard measurement of the material properties of the LC that we can use as a reference for the deformations, stresses, and strains presented herein. As a result, the stress and strain values reported for the various tissues may not reflect the *in vivo* condition, although the regional distributions and relative contribution of IOP and CSFP to the stress and strain patterns that are the focus of the manuscript should be valid. Similarly, there are no experimental data on the stresses and strains in the LC beams and laminar NT in the sitting and supine body positions that we could use to validate our results. Hence, we assumed that the LC material properties were consistent with these models from our prior work^{62,63} in which LC properties were assigned based on matching the LC deformations to the range reported in the literature.^{33,85,103,104}

Second, although the 3D reconstruction methodology that forms the morphological basis for the LC microstructure, sclera, and pia geometries is consistent with the tissue morphology *in vivo*,¹⁰⁵ there is some artifact due to tissue processing, fixation, and embedding for histologic reconstruction.¹⁰⁵

Third, the vascular trunk in the laminar region might influence the mechanics of the ONH *in vivo*. Although we include the central retinal vessel trunks in our ONH FE models, they are not pressurized with blood, which will be addressed in future studies in which hydrostatic pressure and compressive strain mapping will be incorporated as surrogates for capillary and vessel perfusion.

Fourth, although the original images of the LC beams had a pixel size of approximately 1.5 μm , the element edge length of the LC and NT in the FE model was set to approximately 5 to 12 μm . Whereas the remeshing led to slight alterations in the area and volume of the LC in the ONH FE

model, our published comparative analyses exhibited negligible effects on LC stresses and strains.⁶²

Fifth, although the loading boundary was quasi-static in LS-DYNA, the material parameters did not include viscoelasticity that perhaps are important over extended time periods in ocular tissues.^{106,107} Loading was imposed over 500 ms to reflect the physiologic condition, which could benefit from including the viscoelastic effects in the material model in future studies. Future analyses will include a viscoelastic solid matrix material formulation in cases in which the time course of the loading is longer and thus likely to involve viscoelasticity. In addition, the scleral and pia material formulation does not model collagen fibril crimp explicitly, although it accurately captures the heterogeneous anisotropic hyperelastic behavior of these tissues that are the physical manifestations of fibril anisotropy and crimp. It will be important to model the collagen crimp directly in future studies in which crimping parameters are important outcome variables.

Sixth, the same material properties were assigned to all three models and the models were solved under the same boundary and loading conditions. The only difference between the models was the geometry, which allowed us to analyze the effects of morphological variability independent of the material properties and loading and boundary conditions.

Seventh, our 3D ONH reconstructions upon which the models are based were done of eyes that were pressurized to mimic IOP, but no pressure was applied in the subarachnoid space. Hence, the delineations do not include a patent subarachnoid space, and the input geometries do not represent the *in vivo* state in terms of the amount of posterior sclera exposed to CSFP. We are not aware of studies that have measured this area, but it is likely to be small given that the pia and dural sheaths split to form the subarachnoid space at the optic nerve insertion, resulting in a sharp point at the anterior most aspect of the subarachnoid space in most eyes, and leaving very little posterior scleral area exposed to CSFP. In addition, the strain in the dura from the approximately 11 mm Hg change in CSFP simulated herein is likely to be very small, and because soft membranous fibrillar tissues have little resistance to bending, the rotational forces transferred to the posterior scleral flange due to dural sheath expansion are likely to be negligible. Inclusion of the dura would be important if we were simulating ocular motion in which the optic nerve, pia and dura would “pull” or tether the posterior globe at their insertion, but we are only modeling pressure changes with no eye motion. It should be noted that prior modeling studies have shown stress and strain concentrations at the dural sheath insertions into the peripapillary sclera, and that dural sheath modulus has some effect on scleral canal expansion, but this is likely due to their use of linear elastic properties that have an artificially high resistance to bending that is not present in the dural sheath *in vivo*. In this study, we assign hyperelastic anisotropic properties to the load bearing tissues, and whereas this is an improvement over prior approaches, it cannot account for the artificially high resistance to bending present in this material formulation (or others) should we have elected to include the dural sheath. On balance, we believe that including the dural sheath in our models would introduce more artifacts to the results than not including it. In addition, the dura inserts well away from the laminar region of the ONH that is the focus of the work, and so its presence (or lack thereof) is not likely to alter the findings

in this study. Even parametric studies and modeling studies using simplified geometries and linear elastic materials have indicated that dural sheath mechanics do not play a large role in laminar deformation, stress, or strain.⁵³

Eighth, our models do not include the choroid, which is known to change thickness/volume with changes in body position. Choroidal volume change is unlikely to affect ONH biomechanics directly, however, as it is most likely to manifest as a transient change in ocular volume and hence IOP, which is modeled explicitly in this study as a pressure applied directly to the retinal surface (see Fig. 1b). It will be important to include the choroid in future modeling studies where the biomechanics of the retina, prelaminar neural tissues, Bruch's membrane, or RPE are important outcome variables.

Ninth, we modeled the IOP change with body position, as reported in the most recent experimental/clinical study in humans.⁴⁰ Although there is a range of values in the literature, the bulk of the results reported in the current study hinge on deformations, stresses, and strains that are normalized per mm Hg pressure change, which negates any issues arising from small, subject-specific, differences in IOP, or CSFP change with body position.

Finally, this study included models of only three eyes from three human donors, which are not likely to represent the full range of biomechanical responses in the population, although a wide range of scleral thicknesses are represented in this small sample. Even with our small sample, it was sufficient to achieve statistically significant differences in our outcome variables. Future studies elucidating the contributions of age, race, sex, and disease state are necessary to investigate these factors.

CONCLUSIONS

Computational modeling of the biomechanical effects of body posture on the laminar beams and interspersed neural tissues has revealed greater tensile, compressive, and shear stresses and strains in the LC beams and laminar NT due to postural changes. Larger axial forces in the cable elements representing collagen fibers in the PPScl were also associated with the supine position. Stresses in the LC beams were three to five times larger than interspersed laminar NT, confirming that the LC provides structural support to the axons in the ONH. Conversely, strains in the laminar NT were three to five times larger than the adjacent LC beams. Most importantly, IOP drives stress, strain, and deformation in the ONH tissues at two to four times the magnitude of CSFP per mm Hg when both are changing simultaneously with postural transition ($P < 0.05$). Hence, whereas CSFP should provide a direct, one-to-one counterpressure to IOP at the ONH and across the LC, it is three- to four-fold less effective at doing so than the simple $TLP = IOP - CSFP$ relationship would suggest. These findings have implications for understanding of the stresses and strains in the ONH connective tissues due to different body postures and may provide insight into potential therapeutic pathways designed to alter various aspects of the ONH biomechanical response.

Acknowledgments

Supported by the National Institutes of Health Grants R01-EY027924, R01-EY018926, and P30-EY003039 (Bethesda,

Maryland); EyeSight Foundation of Alabama (Birmingham, Alabama); and Research to Prevent Blindness (NY, New York).

CRedit Author Statement: A.K. was responsible for conceptualization, methodology, formal analysis, investigation, and writing of the original draft. R.R. was responsible for conceptualization. S.M.R. was responsible for conceptualization. C.G. was responsible for supervision, writing - review and editing, and funding acquisition. J.C.D. was responsible for conceptualization and experimental design, supervision, writing - review and editing, funding acquisition, and project administration. Approving final version of manuscript was done by all the authors.

Data Availability: The raw/processed data required to reproduce these findings cannot be shared at this time, as the data are part of an ongoing study.

Disclosure: A. Karimi, None; R. RazaghiK, None; S.M. Rahmati, None; C.A. Girkin, None; J.C. Downs, None

References

1. Kass MA, Heuer DK, Higginbotham EJ, et al. The Ocular Hypertension Treatment Study - A randomized trial determines that topical ocular hypotensive medication delays or prevents the onset of primary open-angle glaucoma. *Arch Ophthalmol Chic.* 2002;120:701-713.
2. Weinreb RN, Khaw PT. Primary open-angle glaucoma. *Lancet.* 2004;363:1711-1720.
3. Burgoyne CF, Downs JC, Bellezza AJ, Suh JK, Hart RT. The optic nerve head as a biomechanical structure: a new paradigm for understanding the role of IOP-related stress and strain in the pathophysiology of glaucomatous optic nerve head damage. *Prog Retin Eye Res.* 2005;24:39-73.
4. Sigal IA, Ethier CR. Biomechanics of the optic nerve head. *Exp Eye Res.* 2009;88:799-807.
5. Downs JC. Optic nerve head biomechanics in aging and disease. *Exp Eye Res.* 2015;133:19-29.
6. Quigley HA, Addicks EM. Regional differences in the structure of the lamina cribrosa and their relation to glaucomatous optic nerve damage. *Arch Ophthalmol.* 1981;99:137-143.
7. Quigley HA, Nickells RW, Kerrigan LA, Pease ME, Thibault DJ, Zack DJ. Retinal ganglion cell death in experimental glaucoma and after axotomy occurs by apoptosis. *Invest Ophthalmol Vis Sci.* 1995;36:774-786.
8. Downs JC, Girkin CA. Lamina cribrosa in glaucoma. *Curr Opin Ophthalmol.* 2017;28:113-119.
9. Berdahl JP, Allingham RR, Johnson DH. Cerebrospinal fluid pressure is decreased in primary open-angle glaucoma. *Ophthalmology.* 2008;115:763-768.
10. Berdahl JP, Fautsch MP, Stinnett SS, Allingham RR. Intracranial pressure in primary open angle glaucoma, normal tension glaucoma, and ocular hypertension: a case-control study. *Invest Ophthalmol Vis Sci.* 2008;49:5412-5418.
11. Linden C, Qvarlander S, Johannesson G, et al. Normal-Tension Glaucoma Has Normal Intracranial Pressure: A Prospective Study of Intracranial Pressure and Intraocular Pressure in Different Body Positions. *Ophthalmology.* 2018;125:361-368.
12. Ren R, Jonas JB, Tian G, et al. Cerebrospinal fluid pressure in glaucoma: a prospective study. *Ophthalmology.* 2010;117:259-266.
13. Ren R, Wang N, Zhang X, Cui T, Jonas JB. Trans-lamina cribrosa pressure difference correlated with neuroretinal rim area in glaucoma. *Graefes Arch Clin Exp Ophthalmol.* 2011;249:1057-1063.

14. Ren R, Zhang X, Wang N, Li B, Tian G, Jonas JB. Cerebrospinal fluid pressure in ocular hypertension. *Acta Ophthalmologica*. 2011;89:e142–e148.
15. Yang D, Fu J, Hou R, et al. Optic neuropathy induced by experimentally reduced cerebrospinal fluid pressure in monkeys. *Invest Ophthalmol Vis Sci*. 2014;55:3067–3073.
16. Ficarrotta KR, Passaglia CL. Intracranial pressure modulates aqueous humour dynamics of the eye. *J Physiol*. 2020;598:403–413.
17. Berdahl JP, Yu DY, Morgan WH. The translaminar pressure gradient in sustained zero gravity, idiopathic intracranial hypertension, and glaucoma. *Med Hypotheses*. 2012;79:719–724.
18. Fleischman D, Allingham RR. The role of cerebrospinal fluid pressure in glaucoma and other ophthalmic diseases: A review. *Saudi J Ophthalmol*. 2013;27:97–106.
19. Jonas JB, Wang N, Yang D, Ritch R, Panda-Jonas S. Facts and myths of cerebrospinal fluid pressure for the physiology of the eye. *Prog Retin Eye Res*. 2015;46:67–83.
20. Downs JC, Girkin CA. Lamina cribrosa in glaucoma. *Curr Opin Ophthalmol*. 2017;28:113–119.
21. Morgan WH, Yu DY, Cooper RL, Alder VA, Cringle SJ, Constable IJ. The influence of cerebrospinal fluid pressure on the lamina cribrosa tissue pressure gradient. *Invest Ophthalmol Vis Sci*. 1995;36:1163–1172.
22. Jonas JB, Berenshtein E, Holbach L. Anatomic relationship between lamina cribrosa, intraocular space, and cerebrospinal fluid space. *Invest Ophthalmol Vis Sci*. 2003;44:5189–5195.
23. Balaratnasingam C, Morgan WH, Johnstone V, Pandav SS, Cringle SJ, Yu DY. Histomorphometric measurements in human and dog optic nerve and an estimation of optic nerve pressure gradients in human. *Exp Eye Res*. 2009;89:618–628.
24. Nickells RW, Howell GR, Soto I, John SW. Under pressure: cellular and molecular responses during glaucoma, a common neurodegeneration with axonopathy. *Annu Rev Neurosci*. 2012;35:153–179.
25. Howell GR, Libby RT, Jakobs TC, et al. Axons of retinal ganglion cells are insulted in the optic nerve early in DBA/2J glaucoma. *J Cell Biology*. 2007;179:1523–1537.
26. Resta V, Novelli E, Vozzi G, et al. Acute retinal ganglion cell injury caused by intraocular pressure spikes is mediated by endogenous extracellular ATP. *Eur J Neurosci*. 2007;25:2741–2754.
27. Beckel JM, Argall AJ, Lim JC, et al. Mechanosensitive release of adenosine 5'-triphosphate through pannexin channels and mechanosensitive upregulation of pannexin channels in optic nerve head astrocytes: a mechanism for purinergic involvement in chronic strain. *Glia*. 2014;62:1486–1501.
28. Mulvihill JJE, Raykin J, Snider EJ, et al. Development of a Platform for Studying 3D Astrocyte Mechanobiology: Compression of Astrocytes in Collagen Gels. *Ann Biomed Eng*. 2018;46:365–374.
29. Tehrani S, Johnson EC, Cepurna WO, Morrison JC. Astrocyte processes label for filamentous actin and reorient early within the optic nerve head in a rat glaucoma model. *Invest Ophthalmol Vis Sci*. 2014;55:6945–6952.
30. Morgan WH, Yu DY, Alder VA, et al. The correlation between cerebrospinal fluid pressure and retrolaminar tissue pressure. *Invest Ophthalmol Vis Sci*. 1998;39:1419–1428.
31. Morgan WH, Chauhan BC, Yu DY, Cringle SJ, Alder VA, House PH. Optic disc movement with variations in intraocular and cerebrospinal fluid pressure. *Invest Ophthalmol Vis Sci*. 2002;43:3236–3242.
32. Downs JC, Roberts MD, Burgoyne CF. Mechanical environment of the optic nerve head in glaucoma. *Optometry*. 2008;85:425–435.
33. Agoumi Y, Sharpe GP, Hutchison DM, Nicoleta MT, Artes PH, Chauhan BC. Laminar and prelaminar tissue displacement during intraocular pressure elevation in glaucoma patients and healthy controls. *Ophthalmology*. 2011;118:52–59.
34. Morgan WH, Hazelton ML, Yu DY. Retinal venous pulsation: Expanding our understanding and use of this enigmatic phenomenon. *Prog Retinal Eye Res*. 2016;55:82–107.
35. Anderson DR, Grant WM. The influence of position on intraocular pressure. *Invest Ophthalmol*. 1973;12:204–212.
36. Magnaes B. Body position and cerebrospinal fluid pressure. Part 1: clinical studies on the effect of rapid postural changes. *J Neurosurg*. 1976;44:687–697.
37. Bjørn M. Body position and cerebrospinal fluid pressure. *J Neurosurg*. 1976;44:698–705.
38. Poca MA, Sahuquillo J, Topczewski T, Lastra R, Font ML, Corral E. Posture-induced changes in intracranial pressure: a comparative study in patients with and without a cerebrospinal fluid block at the craniovertebral junction. *Neurosurgery*. 2006;58:899–906.
39. Qvarlander S, Sundström N, Malm J, Eklund A. Postural effects on intracranial pressure: modeling and clinical evaluation. *J Applied Physiol*. 2013;115:1474–1480.
40. Eklund A, Jóhannesson G, Johansson E, et al. The pressure difference between eye and brain changes with posture. *Ann Neurol*. 2016;80:269–276.
41. Jasien JV, Samuels BC, Johnston JM, Downs JC. Effect of Body Position on Intraocular Pressure (IOP), Intracranial Pressure (ICP), and Translaminar Pressure (TLP) Via Continuous Wireless Telemetry in Nonhuman Primates (NHPs). *Invest Ophthalmol Vis Sci*. 2020;61:18.
42. Sheeran P, Bland JM, Hall GM. Intraocular pressure changes and alterations in intracranial pressure. *Lancet*. 2000;355:899.
43. Sajjadi SA, Harirchian MH, Sheikhabaei N, Mohebbi MR, Malekmadani MH, Saberi H. The relation between intracranial and intraocular pressures: study of 50 patients. *Ann Neurol*. 2006;59:867–870.
44. Spentzas T, Henricksen J, Patters AB, Chaum E. Correlation of intraocular pressure with intracranial pressure in children with severe head injuries. *Pediatr Crit Care Med*. 2010;11:593–598.
45. Sigal IA, Yang H, Roberts MD, Burgoyne CF, Downs JC. IOP-induced lamina cribrosa displacement and scleral canal expansion: an analysis of factor interactions using parameterized eye-specific models. *Invest Ophthalmol Vis Sci*. 2011;52:1896–1907.
46. Morgan WH, Lind CR, Kain S, Fatehee N, Bala A, Yu DY. Author response: retinal vein pulsation is in phase with intracranial pressure and not intraocular pressure. *Invest Ophthalmol Vis Sci*. 2012;53:6880.
47. Sigal IA, Grimm JL, Jan NJ, Reid K, Minckler DS, Brown DJ. Eye-specific IOP-induced displacements and deformations of human lamina cribrosa. *Invest Ophthalmol Vis Sci*. 2014;55:1–15.
48. Fazio MA, Clark ME, Bruno L, Girkin CA. In vivo optic nerve head mechanical response to intraocular and cerebrospinal fluid pressure: imaging protocol and quantification method. *Sci Rep*. 2018;8:12639.
49. Feola AJ, Myers JG, Raykin J, et al. Finite Element Modeling of Factors Influencing Optic Nerve Head Deformation Due to Intracranial Pressure. *Invest Ophthalmol Vis Sci*. 2016;57:1901–1911.
50. Tran H, Grimm J, Wang B, et al. Mapping in-vivo optic nerve head strains caused by intraocular and intracranial pressures. *Optical Elastography and Tissue*

Biomechanics IV: International Society for Optics and Photonics; 2017:100670B.

51. Wang B, Tran H, Smith MA, et al. In-vivo effects of intraocular and intracranial pressures on the lamina cribrosa microstructure. *PLoS One*. 2017;12:e0188302.
52. Feola AJ, Coudrillier B, Mulvihill J, et al. Deformation of the lamina cribrosa and optic nerve due to changes in cerebrospinal fluid pressure. *Invest Ophthalmol Vis Sci*. 2017;58:2070–2078.
53. Hua Y, Voorhees AP, Sigal IA. Cerebrospinal Fluid Pressure: Revisiting Factors Influencing Optic Nerve Head Biomechanics. *Invest Ophthalmol Vis Sci*. 2018;59:154–165.
54. Zhu Z, Waxman S, Wang B, et al. Interplay between intraocular and intracranial pressure effects on the optic nerve head in vivo. *Exp Eye Res*. 2021;213:108809.
55. Yablonski M, Ritch R, Pokorny K. Effect of decreased intracranial-pressure on optic disk. *Investigative Ophthalmology & Visual Science: LIPPINCOTT-RAVEN PUBL 227 EAST WASHINGTON SQ, PHILADELPHIA, PA 19106*; 1979:165.
56. Girard MJ, Beotra MR, Chin KS, et al. In Vivo 3-Dimensional Strain Mapping of the Optic Nerve Head Following Intraocular Pressure Lowering by Trabeculectomy. *Ophthalmology*. 2016;123:1190–1200.
57. Downs JC, Roberts MD, Sigal IA. Glaucomatous cupping of the lamina cribrosa: a review of the evidence for active progressive remodeling as a mechanism. *Exp Eye Res*. 2011;93:133–140.
58. Stowell C, Burgoyne CF, Tamm ER, et al. Biomechanical aspects of axonal damage in glaucoma: A brief review. *Exp Eye Res*. 2017;157:13–19.
59. Tamm ER, Ethier CR, Dowling JE, et al. Biological aspects of axonal damage in glaucoma: A brief review. *Exp Eye Res*. 2017;157:5–12.
60. Resta V, Novelli E, Vozzi G, et al. Acute retinal ganglion cell injury caused by intraocular pressure spikes is mediated by endogenous extracellular ATP. *Eur J Neurosci*. 2007;25:2741–2754.
61. Beckel JM, Argall AJ, Lim JC, et al. Mechanosensitive Release of Adenosine 5'-triphosphate Through Pannexin Channels and Mechanosensitive Upregulation of Pannexin Channels in Optic Nerve Head Astrocytes: A Mechanism for Purinergic Involvement in Chronic Strain. *Glia*. 2014;62:1486–1501.
62. Karimi A, Rahmati SM, Grytz RG, Girkin CA, Downs JC. Modeling the biomechanics of the lamina cribrosa microstructure in the human eye. *Acta Biomater*. 2021;134:357–378.
63. Karimi A, Rahmati SM, Razaghi R, Girkin CA, Crawford Downs J. Finite element modeling of the complex anisotropic mechanical behavior of the human sclera and pia mater. *Comput Methods Programs Biomed*. 2022;215:106618.
64. Karimi A, Grytz R, Rahmati SM, Girkin CA, Downs JC. Analysis of the effects of finite element type within a 3D biomechanical model of a human optic nerve head and posterior pole. *Computer Methods and Programs in Biomedicine*. 2021;198:105794.
65. Karimi A, Razaghi R, Girkin CA, Downs JC. Ocular biomechanics during improvised explosive device blast: a computational study using eye-specific models. *Injury*. 2022;53(4):1401–1415.
66. Girkin CA, Fazio MA, Yang H, et al. Variation in the three-dimensional histomorphometry of the normal human optic nerve head with age and race: lamina cribrosa and peripapillary scleral thickness and position. *Invest Ophthalmol Vis Sci*. 2017;58:3759–3769.
67. Grau V, Downs JC, Burgoyne CF. Segmentation of trabeculated structures using an anisotropic Markov random field: application to the study of the optic nerve head in glaucoma. *IEEE Trans Med Imag*. 2006;25:245–255.
68. Gogola A, Jan NJ, Lathrop KL, Sigal IA. Radial and Circumferential Collagen Fibers Are a Feature of the Peripapillary Sclera of Human, Monkey, Pig, Cow, Goat, and Sheep. *Invest Ophthalmol Vis Sci*. 2018;59:4763–4774.
69. Hallquist JO. LS-DYNA Keyword User's Manual volume I. *LSTC, Version 971 volumes 1 and 2*. 2009. Available at: https://lstc.com/pdf/ls-dyna_971_manual_k.pdf, word User's Manual (Version 971) - Volumes I and II (lstc.com).
70. Hallquist JO. LS-DYNA Keyword User's Manual Volume II Material Models. *Livermore, California, USA* 2013. Available at: https://ftp.lstc.com/anonymous/outgoing/jday/manuals/LS-DYNA_manual_Vol_II_R7.1.pdf, ORD USER'S MANUAL - VOLUME I I - MATERIAL MODELS - R7.1 (lstc.com).
71. Hayashi S, Chen H, Hu W. Development of new simulation technology for compression molding of long fiber reinforced plastics. *Proceedings of the 15th International LS-DYNA Users Conference, Detroit, MI, USA; 2018: June 10–12, 2018*. Available at: <https://www.dynalook.com/conferences/15th-international-ls-dyna-conference/composites/development-of-new-simulation-technology-for-compression-molding-of-long-fiber-reinforced-plastics-using-ls-dyna-r-ls-dyna-r>, (dynalook.com).
72. Hayashi S, Chen H, Hu W. Development of New Simulation Technology for Compression Molding of Long Fiber Reinforced Plastics using LS-DYNA. *Proc 15th International LS-DYNA Conference; June 10–12, 2018*. Available at: development-of-new-simul, <https://www.dynalook.com/conferences/15th-international-ls-dyna-conference/composites/development-of-new-simulation-technology-for-compression-molding-of-long-fiber-reinforced-plastics-using-ls-dyna-r>, (dynalook.com).
73. Hayashi S, Wu C, Hu W, Wu Y, Pan X, Chen H. New Methods for Compression Molding Simulation and Component Strength Validation for Long Carbon Fiber Reinforced Thermoplastics. *12th European LS-DYNA Conference 2019, Koblenz, Germany; 2019*. Available at: https://www.dynalook.com/conferences/12th-european-ls-dyna-conference-2019/fiber-reinforced-polymers/hayashi_jsol.pdf, (dynalook.com).
74. Rahmati SM, Razaghi R, Karimi A. Biomechanics of the keratoconic cornea: Theory, segmentation, pressure distribution, and coupled FE-optimization algorithm. *J Mech Behav Biomed Mater*. 2021;113:104155.
75. Turner DC, Edmiston AM, Zohner YE, et al. Transient Intraocular Pressure Fluctuations: Source, Magnitude, Frequency, and Associated Mechanical Energy. *Invest Ophthalmol Vis Sci*. 2019;60:2572–2582.
76. Scheffe H. A method for judging all contrasts in the analysis of variance. *Biometrika*. 1953;40:87–110.
77. Lee DS, Lee EJ, Kim T-W, et al. Influence of Translaminar Pressure Dynamics on the Position of the Anterior Lamina Cribrosa Surface. *Invest Ophthalmol Vis Sci*. 2015;56:2833–2841.
78. Jonas JB, Wang N. Cerebrospinal fluid pressure and glaucoma. *J Ophthalmic Vis Res*. 2013;8:257–263.
79. Yang D, Fu J, Hou R, et al. Optic neuropathy induced by experimentally reduced cerebrospinal fluid pressure in monkeys. *Invest Ophthalmol Vis Sci*. 2014;55:3067–3073.
80. Marek B, Harris A, Kanakamedala P, et al. Cerebrospinal fluid pressure and glaucoma: regulation of trans-lamina cribrosa pressure. *Br J Ophthalmol*. 2014;98:721–725.
81. Mari JM, Strouthidis NG, Park SC, Girard MJ. Enhancement of lamina cribrosa visibility in optical coherence

- tomography images using adaptive compensation. *Invest Ophthalmol Vis Sci.* 2013;54:2238–2247.
82. Girard MJ, Tun TA, Husain R, et al. Lamina cribrosa visibility using optical coherence tomography: comparison of devices and effects of image enhancement techniques. *Invest Ophthalmol Vis Sci.* 2015;56:865–874.
 83. Jonas JB, Fernandez MC, Sturmer J. Pattern of glaucomatous neuroretinal rim loss. *Ophthalmology.* 1993;100:63–68.
 84. Midgett DE, Jefferys JL, Quigley HA, Nguyen TD. The inflation response of the human lamina cribrosa and sclera: Analysis of deformation and interaction. *Acta Biomaterialia.* 2020;106:225–241.
 85. Midgett DE, Pease ME, Jefferys JL, et al. The pressure-induced deformation response of the human lamina cribrosa: analysis of regional variations. *Acta Biomaterialia.* 2017;53:123–139.
 86. Sigal IA, Yang H, Roberts MD, et al. IOP-induced lamina cribrosa deformation and scleral canal expansion: independent or related? *Invest Ophthalmol Vis Sci.* 2011;52:9023–9032.
 87. Mao Y, Yang D, Li J, et al. Finite element analysis of trans-lamina cribrosa pressure difference on optic nerve head biomechanics: the Beijing Intracranial and Intraocular Pressure Study. *Sci China Life Sci.* 2020;63:1887–1894.
 88. Floyd MS, Katz BJ, Digre KB. Measurement of the scleral canal using optical coherence tomography in patients with optic nerve drusen. *Am J Ophthalmol.* 2005;139:664–669.
 89. Zhang Z, Wang X, Jonas JB, et al. Valsalva manoeuvre, intraocular pressure, cerebrospinal fluid pressure, optic disc topography: Beijing intracranial and intra-ocular pressure study. *Acta Ophthalmol.* 2014;92:e475–e480.
 90. Kim YW, Lee DH, Lim HB, et al. Age-Dependent Variation of Lamina Cribrosa Displacement During the Standardized Valsalva Maneuver. *Sci Rep.* 2019;9:6645.
 91. Kedar S, Tong J, Bader J, et al. Effects of Acute Intracranial Pressure Changes on Optic Nerve Head Morphology in Humans and Pig Model. *Curr Eye Res.* 2022;47(2):304–311.
 92. Zhu ZY, Waxman S, Wang B, et al. Interplay between intraocular and intracranial pressure effects on the optic nerve head in vivo. *Exp Eye Res.* 2021;213:108809.
 93. Downs JC, Ensor ME, Bellezza AJ, Thompson HW, Hart RT, Burgoyne CF. Posterior scleral thickness in perfusion-fixed normal and early-glaucoma monkey eyes. *Invest Ophthalmol Vis Sci.* 2001;42:3202–3208.
 94. Downs JC, Blidner RA, Bellezza AJ, Thompson HW, Hart RT, Burgoyne CF. Peripapillary scleral thickness in perfusion-fixed normal monkey eyes. *Invest Ophthalmol Vis Sci.* 2002;43:2229–2235.
 95. Girard M, Suh J-K, Bottlang M, Burgoyne C, Downs J. Age-Related Alterations in the 3D, Nonlinear, Anisotropic Mechanical Properties of Non-Human Primate (NHP) Posterior Sclera. *Invest Ophthalmol Vis Sci.* 2008;49:4058.
 96. Sigal IA, Flanagan JG, Ethier CR. Factors influencing optic nerve head biomechanics. *Invest Ophthalmol Vis Sci.* 2005;46:4189–4199.
 97. Burgoyne CF. A biomechanical paradigm for axonal insult within the optic nerve head in aging and glaucoma. *Exp Eye Res.* 2011;93:120–132.
 98. Bellezza AJ, Rintalan CJ, Thompson HW, Downs JC, Hart RT, Burgoyne CF. Deformation of the lamina cribrosa and anterior scleral canal wall in early experimental glaucoma. *Invest Ophthalmol Vis Sci.* 2003;44:623–637.
 99. Yang H, Downs JC, Girkin C, et al. 3-D histomorphometry of the normal and early glaucomatous monkey optic nerve head: lamina cribrosa and peripapillary scleral position and thickness. *Invest Ophthalmol Vis Sci.* 2007;48:4597–4607.
 100. Strouthidis NG, Fortune B, Yang H, Sigal IA, Burgoyne CF. Longitudinal change detected by spectral domain optical coherence tomography in the optic nerve head and peripapillary retina in experimental glaucoma. *Invest Ophthalmol Vis Sci.* 2011;52:1206–1219.
 101. Morgan WH, Yu DY, Balaratnasingam C. The role of cerebrospinal fluid pressure in glaucoma pathophysiology: the dark side of the optic disc. *J Glaucoma.* 2008;17:408–413.
 102. Morgan WH, Lind CR, Kain S, Fatehee N, Bala A, Yu D-Y. Retinal vein pulsation is in phase with intracranial pressure and not intraocular pressure. *Invest Ophthalmol Vis Sci.* 2012;53:4676–4681.
 103. Midgett DE, Quigley HA, Nguyen TD. In vivo characterization of the deformation of the human optic nerve head using optical coherence tomography and digital volume correlation. *Acta Biomaterialia.* 2019;96:385–399.
 104. Midgett DE, Jefferys JL, Quigley HA, Nguyen TD. The inflation response of the human lamina cribrosa and sclera: Analysis of deformation and interaction. *Acta Biomaterialia.* 2020;106:225–241.
 105. Fazio MA GS, Bruno L, Bianco G, et al. Histologic Validation of Optical Coherence Tomography-Based Three-Dimensional Morphometric Measurements of the Human Optic Nerve Head: Methodology and Preliminary Results. *Exp Eye Res.* 2021;205:108475.
 106. Downs JC, Suh JK, Thomas KA, Bellezza AJ, Burgoyne CF, Hart RT. Viscoelastic characterization of peripapillary sclera: material properties by quadrant in rabbit and monkey eyes. *J Biomech Eng.* 2003;125:124–131.
 107. Downs JC, Suh JK, Thomas KA, Bellezza AJ, Hart RT, Burgoyne CF. Viscoelastic material properties of the peripapillary sclera in normal and early-glaucoma monkey eyes. *Invest Ophthalmol Vis Sci.* 2005;46:540–546.